**Astronomy
&
Astrophysics**

Strong pulses detected from rotating radio transient J1819−1458

H. D. Hu[1,2], A. Esamdin[1], J. P. Yuan[1], Z. Y. Liu[1], R. X. Xu[3], J. Li[1,2], G. C. Tao[1,2], and N. Wang[1]

[1] Urumqi Observatory, NAOC, 40-5 South Beijing Road, Urumqi 830011, P.R. China
    e-mail: aliyi@uao.ac.cn
[2] Graduate University of Chinese Academy of Sciences, 19A Yuquan Road, Beijing 100049, P.R. China
[3] School of Physics and State Key Laboratory of Nuclear Physics and Technology, Peking University, Beijing 100871, P.R. China

ABSTRACT

Aims. We analyze individual pulses detected from RRAT J1819−1458.
Methods. From April 2007 to April 2010, we carried out observations using the Nanshan 25-m radio telescope of Urumqi Observatory at a central frequency of 1541.25 MHz.
Results. We obtain a dispersion measure $DM = 195.7 \pm 0.3$ pc cm^{-3} by analyzing all the 423 detected bursts. The tri-band pattern of arrival time residuals is confirmed by a single pulse timing analysis. Twenty-seven bimodal bursts located in the middle residual band are detected, and, profiles of two typical bimodal bursts and two individual single-peak pulses are presented. We determine the statistical properties of SNR and W_{50} of bursts in different residual bands. The W_{50} variation with SNR shows that the shapes of bursts are quite different from each other. The cumulative probability distribution of intensity for a possible power law with index $\alpha = 1.6 \pm 0.2$ is inferred from the number of those bursts with $SNR \geq 6$ and high intensities.

Key words. stars: neutron – pulsars: individual: J1819−1458

1. Introduction

Rotating radio transients (RRATs) are a recently discovered class of neutron stars. At a wave band ∼1.4 GHz, they have sporadic radio pulses of durations ranging from 0.5 to 100 ms with flux densities from ∼10 mJy to ∼10 Jy and burst rates from 0.3 to 50.3 per hour. The study of the time of arrival (TOA) of single pulses indicates that these RRATs have periods ranging from 0.1 to 7 s and surface magnetic field of ∼10^{12} or ∼10^{13} Gauss (McLaughlin et al. 2006; Deneva et al. 2009; McLaughlin et al. 2009; Burke-Spolaor & Bailes 2010; Keane et al. 2010).

J1819−1458 is the brightest and most prolific radio transient among the more than forty known RRATs. The dispersion measure of the source is $DM \approx 196$ pc cm^{-3}. At 1.4 GHz, the durations of most bursts are ∼3 ms at intervals of ∼3 min and the peak flux density is ∼10 Jy (McLaughlin et al. 2006; Esamdin et al. 2008; Lyne et al. 2009). The irregular bursts cannot be detected by standard periodicity search methods, but a single pulse TOA analysis is capable of identifying the rotation period of $P \approx 4.26$ s with a spin-down rate $\dot{P} \approx 5.76 \times 10^{-13}$ s s^{-1}. The inferred surface magnetic field density is $B_s \approx 5 \times 10^{13}$ Gauss and characteristic age is $\tau_c \approx 1.2 \times 10^5$ years (McLaughlin et al. 2006; Esamdin et al. 2008). Lyne et al. (2009) reported two unusual glitches with quite different post-glitch behavior and an associated increase in the flux intensity, which implies that RRAT J1819−1458 may be moving toward the death line in the pulsar $P - \dot{P}$ diagram. The Faraday rotation measure of RRAT J1819−1458 is $RM \approx 330 \pm 30$ rad m^{-2} and the integrated linear polarization measurement is relatively low owing to orthogonal modes of polarization, although some individual pulses are highly polarized (Karastergiou et al. 2009).

After the *Chandra X-ray Observatory* detected the X-ray counterpart (Reynolds et al. 2006; Gaensler et al. 2007), the *XMM-Newton* discovered the X-ray pulsation aligned with the phase of the radio pulse and a possible X-ray spectral feature that is similar to those of the X-ray dim isolated neutron stars (XDINS, cf. Popov et al. 2006; Haberl 2007; Kondratiev et al. 2009). This indicates that RRAT J1819−1458 is a cooling neutron star and possibly a transitional object between the pulsar and magnetar classes (McLaughlin et al. 2007; for descriptions of magnetars, see Woods & Thompson 2006; Mereghetti 2008). Rea et al. (2009) found the X-ray extended emission around RRAT J1819−1458, which can be interpreted as being a nebula powered by the pulsar. The near-infrared counterpart to the extended X-ray emission was not detected in the observation taken by Rea et al. (2010). There is no evidence of the optical counterpart to the RRAT in the observation implemented by Dhillon et al. (2006), but there is possibly a near-infrared counterpart (Rea et al. 2010).

Weltevrede et al. (2006) assumed that some RRATs could be explained in terms of normal pulsars that have pulse amplitude modulations, such as PSR B0656+14. Had they been put at properly large distances, their weak pulses would have been undetectable and they might have been identified as RRATs. From the observation results of PSR J1119−6127 with magnetic field strength and post-glitch behavior similar to those of RRAT J1819−1458, it is understood that some RRATs can be interpreted as the consequences of the line of sight missing the steady pulse components of emission area and intercepting these unstable ones (Weltevrede et al. 2011). Wang et al. (2007) proposed that RRATs could not be directly related to nulling pulsars because the latter have no observed pulses such as giant pulses (e.g. Hankins et al. 2003; Knight et al. 2006). However, taking PSR J0941−39 as an example, Burke-Spolaor & Bailes (2010) argued that there was possibly a link between RRATs and pulsars with nulling phenomena. There is also a hypothesis that some RRATs are possibly related to radio pulsing magnetars such as XTE J1810−197 (Serylak et al. 2009). By studying the birthrates

of neutron stars, RRATs have been considered distant XDINS (Popov et al. 2006) or an evolutionary stage of a single class of objects (Keane & Kramer 2008). In the $P - \dot{P}$ diagram, the periods of known RRATs cover a large range where periods of normal pulsars and magnetars distribute; the observational characteristics of RRATs vary with diversities (McLaughlin et al. 2009). Although there have been several theoretical interpretations of RRATs (e.g. Li 2006; Zhang et al. 2007; Luo & Melrose 2007; Cordes & Shannon 2008; Ouyed et al. 2009), RRATs do not appear to be completely understood.

This paper presents a study of individual bursts detected in single pulse observations from April 2007 to April 2010. Section 2 describes the observation details. The results of study on detected pulses are given in Sect. 3 and discussed in Sect. 4. Section 5 briefly summarizes this paper.

2. Observations

Observations were performed using the Nanshan 25-m radio telescope of Urumqi Observatory. The antenna has a cryogenic receiver of two orthogonal linear polarization channels with a central frequency of 1541.25 MHz. Each polarization channel consists of 128 sub-channels of bandwidth 2.5 MHz and has a total bandwidth of 320 MHz. The signal from each sub-channel is 1-bit sampled and recorded to hard disk for subsequent offline processing (for more details of the system, see Wang et al. 2001). The minimum detectable flux density $S_{\min} \approx 3.4$ Jy is limited by

$$S_{\min} = \frac{2\alpha\beta k T_{\mathrm{sys}}}{\eta A \sqrt{n_{\mathrm{p}}\tau\Delta f}}, \qquad (1)$$

in which $\alpha = 5$ is the threshold signal-to-noise ratio (SNR), $\beta = \sqrt{\pi/2}$ is the loss factor due to 1-bit digitization, k is the Boltzmann constant, $T_{\mathrm{sys}} = T_{\mathrm{rec}} + T_{\mathrm{spl}} + T_{\mathrm{sky}} \approx 32$ K is the system temperature, $\eta \approx 57\%$ is the telescope efficiency at 1541.25 MHz, $A = 490.9$ m^2 is the telescope area, $n_{\mathrm{p}} = 2$ is the number of polarization channels, $\tau = 0.5$ ms is the sampling interval, and $\Delta f = 320$ MHz is the total bandwidth (Manchester et al. 2001).

From Apr. 10, 2007 to Apr. 13, 2010, 260 hours of data were accumulated in 1100 days of observations. The time-span of each observation session was 2 h.

3. Data analysis and results

Pulsed radio waves propagating through the ionized plasma of the interstellar media are dispersed because the group velocity in the media is frequency dependent. This demonstrates that the higher frequency components of a radio pulse arrive before those at lower frequencies. To achieve a higher SNR and narrower (normally closer to the real) profile of the pulse, the time delay must be removed. The time difference between the two components of different frequencies, Δt, is given by

$$\Delta t = 4.1488 \times DM \times \left(\frac{1}{f_1^2} - \frac{1}{f_h^2} \right) \text{ ms}, \qquad (2)$$

where DM is the dispersion measure in pc cm^{-3}, and f_1 and f_h are the values (in GHz) of the lower and higher frequencies, respectively (Lorimer & Kramer 2005, Appendix 2.4). We use Eq. (2) with the nominal DM value of $DM = 196$ pc cm^{-3} to calculate and remove the delayed time of signal between the sub-channel at the lowest frequency and sub-channels at other
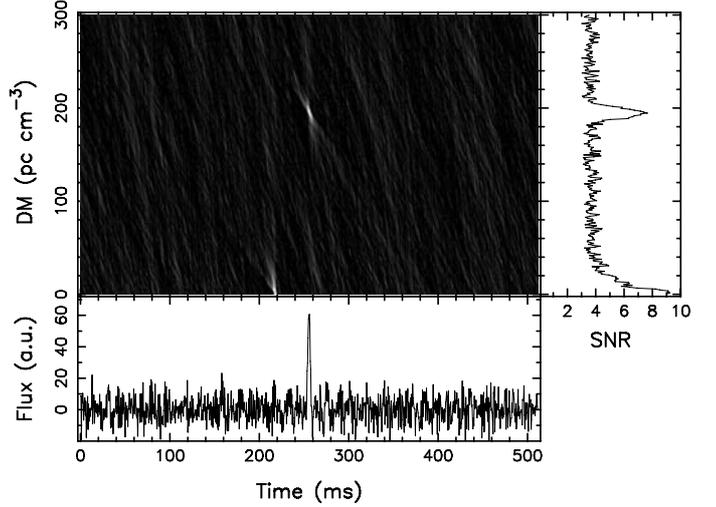

Fig. 1. Diagnostic plot showing detected burst from RRAT J1819−1458 and RFI signal. The *upper-left panel* is a DM-time gray map generated by de-dispersing the signal with DM varying from 0.7 to 300.7 pc cm^{-3} in steps of 1 pc cm^{-3}. The brightness of the plot indicates the amplitude at the corresponding position, and, the two bright marks at around $DM = 195.7$ and $DM = 0$ pc cm^{-3} represent the burst and RFI. The *upper-right panel* is a DM–*SNR* graph with two peak *SNR* values at around $DM = 195.7$ and $DM = 0$ pc cm^{-3}, in which the *SNR* for each DM is calculated from the bin of maximum amplitude over 512 ms. The *lower-left panel* is a time series graph showing the amplitude (in an arbitrary unit) of each bin at $DM = 195.7$ pc cm^{-3}, which clearly delineates a narrow burst profile at the center.

frequencies, finding that the signals from two polarization channels are de-dispersed. The signals of all 256 sub-channels are summed, and signals of $SNR \geq 5$ are searched for in the whole time series of each observation. Selected signals with SNR above the threshold are reprocessed with DM varying from 0.7 to 300.7 pc cm^{-3} in steps of 1 pc cm^{-3}. To each DM, the SNR of the bin with the maximum amplitude is computed over 1024 bins (512 ms), with the candidate burst being at the center of the series. Through the process, a diagnostic plot shown in Fig. 1 is generated and used for careful inspection by eye to identify real bursts (for more details of the burst detection method adopted, see Esamdin et al. 2008).

In the upper-left panel of Fig. 1, we present a DM-time gray map that obviously shows two white marks. The mark at around the intersection point of the line of $DM = 195.7$ pc cm^{-3} and center line of the time series represents a burst detected from RRAT J1819−1458, and the one at about 210 ms around $DM = 0$ pc cm^{-3} represents a signal of radio frequency interference (RFI, see Cordes & McLaughlin 2003) that sometimes contaminates the observation data. The mark representing the burst dissolves as the DM increases or decreases from the nominal DM, whereas the one representing the RFI dissolves as the DM increases from 0 pc cm^{-3}. The upper-right panel is a DM–*SNR* line graph illustrating the SNR variation with DM, where the SNR is from the bin of maximum amplitude in the 512 ms time series for every DM value. As illustrated, the SNR has two peak values at around $DM = 195.7$ pc cm^{-3} for the burst and $DM = 0$ pc cm^{-3} for the RFI, and far away from these two DM values, the SNR varies like white noise. The lower-left panel shows the time series at $DM = 195.7$ pc cm^{-3} and clearly displays a burst profile in the center. A typical burst detected from RRAT J1819−1458 has the visual characteristics presented in Fig. 1, which is a significant criterion for identifying a real burst.
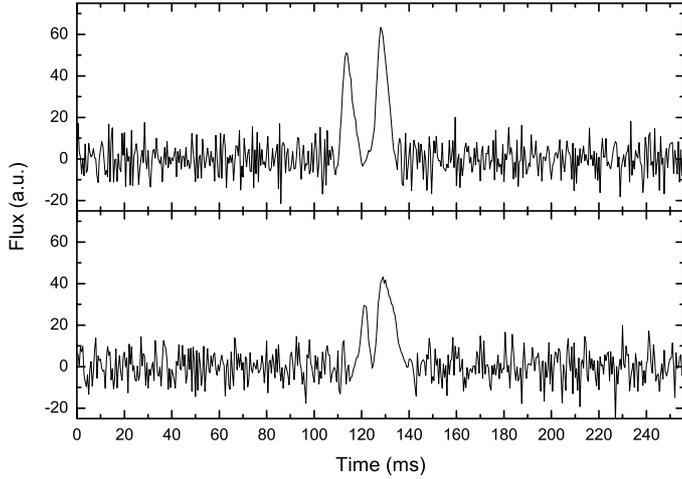
Fig. 3. Variation of average *SNR* with DM. The average *SNR* that has a peak value at $DM = 195.7$ pc cm^{-3} as indicated by the arrow, is calculated from all 423 detected bursts from RRAT J1819−1458 with *DM* increasing from 192 to 199.5 pc cm^{-3} in steps of 0.1 pc cm^{-3}.

Fig. 2. Profiles of two typical bimodal bursts detected from RRAT J1819−1458 where flux density is given in arbitrary unit. The higher *SNR* of the two peaks in each bimodal bursts are 9.2 and 6.5 in the top and bottom panels, respectively. Distances between the two peaks and W_{50} of peaks with the higher *SNR* in each bimodal burst are 14.5 and 4.5 ms in the top panel and 8 and 7.2 ms in the bottom panel.

Using the above method, 423 strong pulses of *SNR* ranging from 5 to 13.3 and durations from 0.5 to 13.7 ms are detected. As Esamdin et al. (2008) noted that five bimodal bursts were detected, there are 27 bimodal bursts detected with distances between two component peaks ranging from 3 to 15 ms, *SNR* from 5.5 to 9.5, and full widths at half maximum (*FWHM*, W_{50}) from 1.3 to 7.2 ms. For a bimodal burst, the *SNR* means the higher *SNR* of the two peaks and the W_{50} is calculated from the peak of the higher *SNR*.

The W_{50} of a burst is obtained from

$$W_{50} = \sqrt{W_{50,\mathrm{obs}}^2 - t_{\mathrm{samp}}^2 - t_{\mathrm{DM}}^2 - t_{\mathrm{scatt}}^2}, \tag{3}$$

in which $W_{50,\mathrm{obs}}$ is the observed *FWHM*, $t_{\mathrm{samp}} = 0.5$ ms is the sampling interval, $t_{\mathrm{DM}} = 1.109$ ms is the dispersion smearing time across one sub-channel, and $t_{\mathrm{scatt}} = 0.015$ ms is the broadening of the pulse due to interstellar scattering. Both t_{DM} and t_{scatt} are given by

$$t_{\mathrm{DM}} = 8.2976 \times 10^6 \times DM \times f_{\mathrm{c}}^{-3} \times B \text{ ms} \tag{4}$$

and

$$t_{\mathrm{scatt}} = \left(\frac{DM}{1000}\right)^{3.5} \times \left(\frac{400}{f_{\mathrm{c}}}\right)^4 \times 10^3 \text{ ms}, \tag{5}$$

where $DM = 195.7$ pc cm^{-3} is the dispersion measure, $f_{\mathrm{c}} = 1541.25$ MHz is the central frequency of the receiver channel, and $B = 2.5$ MHz is the sub-channel bandwidth (Lyne & Graham-Smith 2006; Lorimer & Kramer 2005).

Figure 2 portrays two profiles of typical detected bimodal bursts from RRAT J1819−1458 with the distances between their two peaks being 14.5 and 8 ms. In Fig. 2, the *SNR* and W_{50} are 9.2 and 4.5 ms in the top panel, and, 6.5 and 7.2 ms in the bottom panel. The peaks of the higher *SNR* appear behind those of the lower *SNR*, as shown in Fig. 2, in 16 bimodal bursts, while peaks of the lower *SNR* appear behind those of the higher *SNR* in another nine bimodal bursts. In the remaining two bimodal bursts, the two peaks visibly have approximately equal *SNR*. There are four bimodal bursts that are possibly "tri-modal", which means
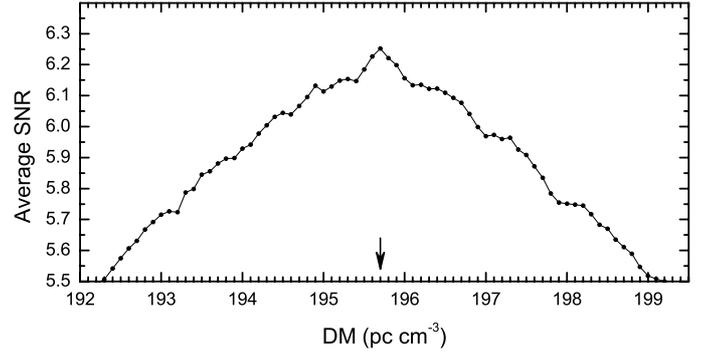
that one burst has possibly three close-set peaks with distances between two adjacent peaks less than 5 ms. However, it is difficult to distinguish the third peak from noise fluctuations because of the low flux density ($SNR \leq 3$).

To obtain a *DM* closer to the intrinsic value, with *DM* increasing from 0 to 400 pc cm^{-3} in steps of 0.1 pc cm^{-3}, average *SNR* of all 423 bursts from RRAT J1819−1458 are calculated for all *DM*. Figure 3 is the graph of average *SNR* versus DM with *DM* varying from 192 to 199.5 pc cm^{-3} and shows that the peak *SNR* is at $DM = 195.7$ pc cm^{-3}. In the range of *DM* from 300 to 400 pc cm^{-3}, where the *SNR* variation behaves like white noise, the standard deviation in the *SNR* fluctuation is 0.023 and its quintuple is 0.115. The *DM* uncertainty is then limited to 0.3 pc cm^{-3} at a 5σ confidence level. The result $DM = 195.7 \pm 0.3$ pc cm^{-3} is in accord with those of McLaughlin et al. (2006) and Esamdin et al. (2008).

In this work, the flux intensity of a detected burst, *E*, is quantified by

$$E = W_{50} \times S, \tag{6}$$

in which W_{50} is the *FWHM* and *S* the peak flux density. The epochs of the two glitches associated with increases in flux intensity are beyond the time range of this observation (Lyne et al. 2009). Thus it is not inconsistent that there is no burst with a significant deviation in flux intensity as shown in Fig. 4 (top). From the figure, there is no evidence that the intensity of bimodal bursts undergoes obvious deviation.

As reported by Lyne et al. (2009) and shown in Fig. 4 (bottom), the timing residuals of RRAT J1819−1458 fall into a triband distribution. With TEMPO2[1] in TEMPO1 compatibility mode and using the same method as Lyne et al. (2009), the parameters ν and $\dot{\nu}$ in Table 1 are obtained by fitting the 423 TOAs while increasing and decreasing the TOAs in the top and bottom bands by 45 ms, respectively. Taking the two glitches and different timing epochs into account, the fitted values of ν and $\dot{\nu}$ correspond to those acquired by Lyne et al. (2009). The residuals from fitting only ν and $\dot{\nu}$ have a waveform of amplitude ~30 ms and period of ~2 years. When the residuals are calculated using the unmodified TOAs and the same fitted parameters, the residuals in the two side bands vary along the tracks of invariable distances from the center band; the residual patterns for the three bands are then similar. This shows that the residual wave is not caused by random phases of the bursts but probably by a timing noise of unknown origin. The small residual rms ($\sigma = 7$ ms) in
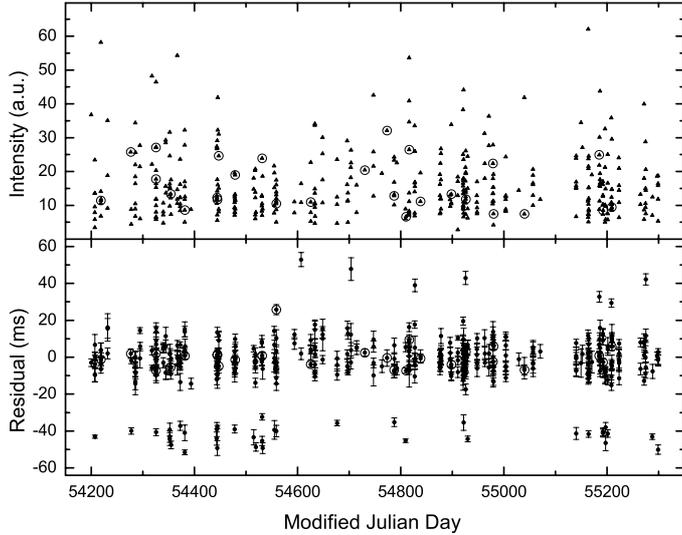
---

[1] http://www.atnf.csiro.au/research/pulsar/tempo2/

Fig. 4. Variation in flux intensity with date (*top*) and timing residuals (*bottom*) for RRAT J1819−1458. The flux intensity is measured in an arbitrary unit and no remarkable deviation of flux density is shown in the variation plot. The timing residuals that show a distribution of three bands with ~40 ms intervals are calculated with the fitted parameters listed in Table 1. The rms of residuals is 17 ms and the error bars are 10σ. Dots with circles in the graphs are the counterparts of bimodal bursts and the gaps in date are due to observation scheduling.

Table 1. Timing parameters of RRAT J1819−1458.

Parameters	Values
RA (J2000)	18:19:34.173
Dec (J2000)	−14:58:03.57
Frequency ν (Hz)	0.234565100209(7)
Frequency derivative $\dot{\nu}$ (Hz s^{-1})	$-3.09123(2) \times 10^{-14}$
Epoch (MJD)	54 321
Dispersion measure DM (pc cm^{-3})	195.7(3)
Time span (MJD)	54200.1–55299.0
Residual rms σ (ms)	7
Fundamental frequency WAVE_OM	0.00437
Number of sinusoids n_H	13

Notes. Numbers in parentheses are uncertainties in the last digits, which are ten times the TEMPO2 standard errors. The position of J1819−1458 is from Rea et al. (2009), of which errors are 0.28 arcsec in both coordinates. With TOAs in the bottom and top residual bands increased and decreased by 45 ms, respectively, σ is calculated by fitting the parameters using the TEMPO2 parameter WAVE_OM to whiten the timing residuals.

Table 1 is due to the modification of TOAs in the top and bottom bands and using the TEMPO2 parameter WAVE_OM to remove red noise from the residuals. The value of WAVE_OM is the fundamental frequency of the removed wave and n_H is the number of the harmonically related sinusoids (for details of the whitening method, see Hobbs et al. 2006). The timing residuals presented in Fig. 4 (bottom) and the rms σ = 17 ms are computed from the unmodified TOAs with parameters that take account of the whitening parameters in Table 1. No successive bursts are simultaneously detected in more than one band over intervals shorter than the spin period and longer than the largest distance of two peaks of the bimodal bursts, which means that no more than one burst is detected in one rotation cycle at this observation sensitivity. The middle emission area is more active and emits about 90% of the bursts detected from RRAT J1819−1458 including the 27 bimodal ones.
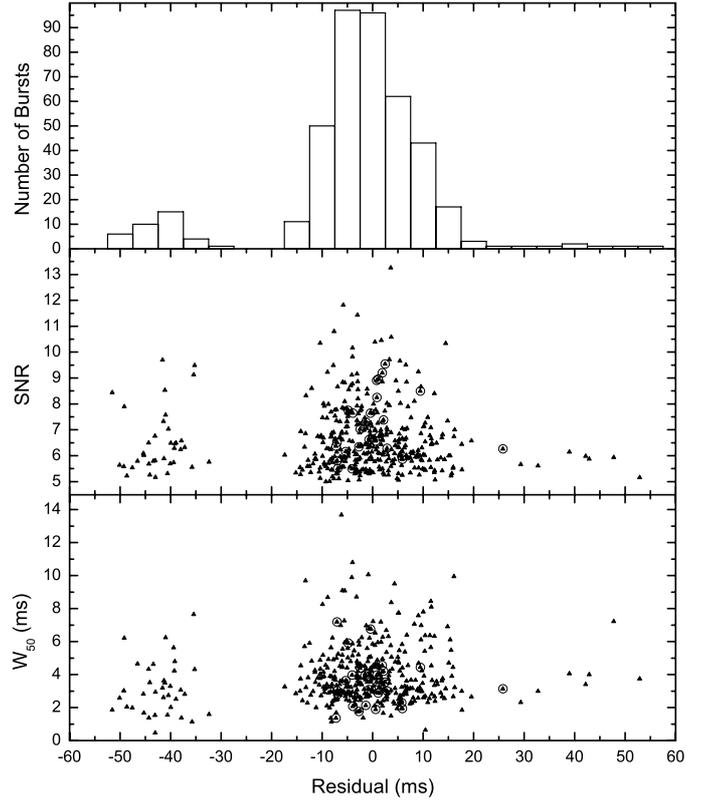
Fig. 5. Distribution of timing residuals of 423 detected bursts from RRAT J1819−1458 (*top*), and, plots of *SNR* (*middle*) and W_{50} (*bottom*) versus timing residual. Circles in the two plots are the counterparts of bimodal bursts.

Figure 5 (top) is the distribution histogram of the timing residuals of 423 detected bursts from RRAT J1819−1458, which shows a tri-modal shape with only seven bursts scattering from ~30 to 55 ms in the last band. This result agrees with the residual distribution reported by Lyne et al. (2009), considering the high detection threshold of the flux density of the Urumqi 25-m telescope and the low *SNR* of bursts in the last band as shown in Fig. 5 (middle). The *SNR* versus timing residual is plotted in Fig. 5 (middle), which shows that the highest *SNR* is from the middle band. The maximum *SNR* of bursts in the last band is ~6 and the mean *SNR* of bursts in the early band is 6.5. It is shown that *SNR* of bursts in the last band are likely to be lower than those in the early band. As displayed in the bottom panel of Fig. 5, the average W_{50} (4.0 ms) of bursts in the last band is slightly larger than that (3.1 ms) of bursts in the early band. When considering the poor quality specimen bursts in the two residual bands, the mean intensity (14.3 in a.u.) of bursts in the last band is approximately equivalent to that (13.0) of bursts in the early band, which is consistent with the result of Lyne et al. (2009, Fig. 2).

The histogram in Fig. 6 is the flux intensity distribution of 266 detected bursts with *SNR* ≥ 6 from RRAT J1819−1458. At higher intensities, the cumulative probability distribution (CPD) of intensity is probably a power law. The power-law index $\alpha = 1.6 \pm 0.2$ with purely formal errors represents the best fit for the number of bursts of intensities higher than 10. The fitting equation is

$$CPD = K \times E^{-\alpha}, \tag{7}$$

where E is the flux intensity in an arbitrary unit (Cognard et al. 1996). Toward both higher and lower intensities, the deviations
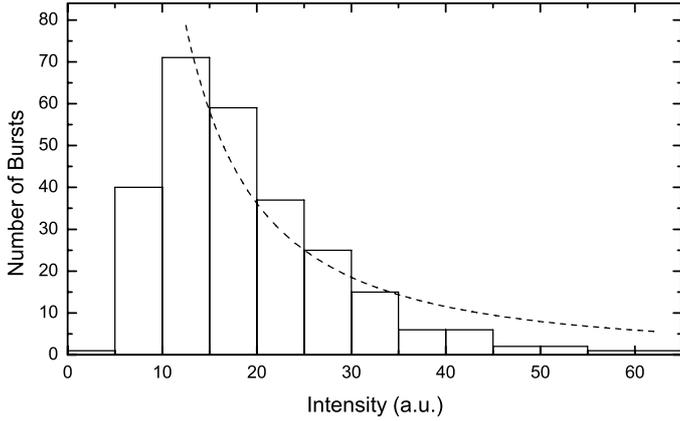
Fig. 6. Flux intensity distribution of bursts detected from RRAT J1819−1458. The flux intensity distribution is generated by 266 detected bursts with $SNR \geq 6$. The dashed curve line signifies that the intensity cumulative probability distribution is a power law. The power-law index $\alpha = 1.6 \pm 0.2$ is fitted from the numbers of bursts with intensities higher than 10.
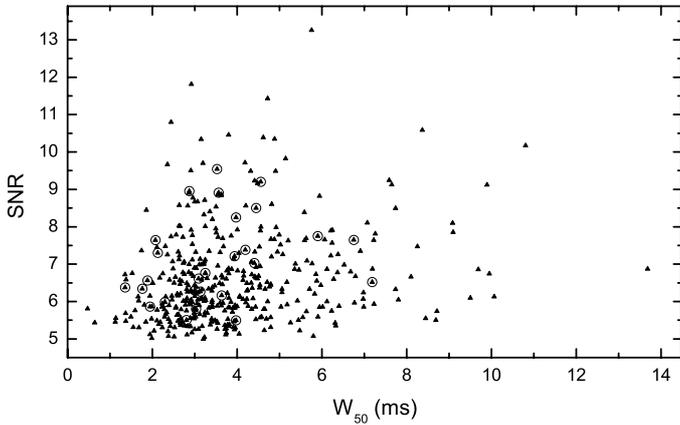

Fig. 7. Plot of SNR versus W_{50} of 423 detected bursts from RRAT J1819−1458. The plot displays that the burst of the highest SNR (13.3) has a medium W_{50} (5.7 ms), whereas the burst with the largest W_{50} (13.7 ms) has a comparatively low SNR (6.9). Circled dots are the counterparts of bimodal bursts.

from fitting curve are possibly due to the small amount of detected bursts of low intensities or/and the CPD actually not being a power law. We infer that it remains unclear whether the CPD is intrinsically a power law.

Figure 7 is a plot of SNR versus W_{50} for all bursts detected from RRAT J1819−1458, which shows that W_{50} widely ranges from 0.5 to 13.7 ms. The variation in SNR that is proportional to the peak flux density has no apparent relation to W_{50}. The widest burst with $W_{50} = 13.7$ ms has a relatively low SNR of 6.9, whereas the brightest burst of $SNR = 13.3$ has a medium W_{50} of 5.7 ms.

Figure 8 portrays two typical examples of detected individual single-peak pulses from RRAT J1819−1458 located in the middle band of timing residuals (shown in Fig. 4) with widely different shapes. The spiky burst of $W_{50} = 2.9$ ms in the top panel has a high SNR of 11.8, whereas the broad burst of $W_{50} = 10.0$ ms in the bottom panel has a rather low SNR of 6.7. As shown in Figs. 7 and 8, profiles of detected bursts have various shapes with W_{50} varying broadly without any clear relation to the peak flux density.
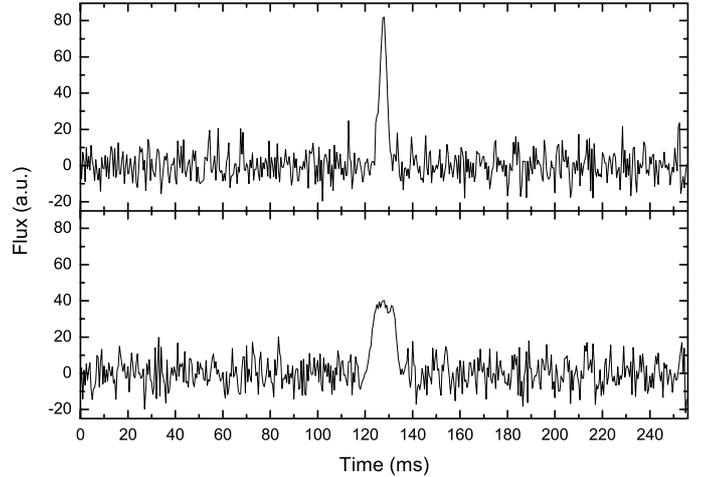

Fig. 8. Profiles of two individual pulses from RRAT J1819−1458 of widely different SNR and W_{50}. The two bursts are located in the middle band of timing residuals. SNR and W_{50} of the burst in the *top panel* are 11.8 and 2.9 ms when those of the burst in the *bottom panel* are 6.7 and 10.0 ms. The amplitude is measured in an arbitrary unit.

4. Discussion

From Figs. 7 and 8, the profiles of the single bursts of RRAT J1819−1458 vary from pulse to pulse. The phenomenon is similar to the one of that individual pulses of a normal pulsar differ from each other (e.g. pulses of PSR B0943+10 as reported by Deshpande & Rankin 1999). Figure 5 (middle) shows that the average SNR of bursts in the last band is lower than those in the early band. This is consistent with the integrated profile from 165 individual bursts in Fig. 3 of Lyne et al. (2009). It is noted that the tri-band pattern of timing residuals could be interpreted in terms of a patchy radio beam with core and conal components (Lyne et al. 2009). Judging from Fig. 5 (bottom), the widths of bursts in the last band are prone to be larger than those of bursts in the early band. It seems that the pulse profiles of bursts in the last and early bands are different, while all the bursts of the two bands are from the "cones". Since the spectrum of the "core" component is always steeper than those of components from the "cones" (Lyne & Manchester 1988), a multi-frequency and higher sensitivity study of bursts from one residual band to another may uncover more knowledge about the phase distribution of individual bursts.

The power-law index of intensity CPD for giant pulses from PSR B1937+21 at 1420 MHz is $\alpha = 1.8$ (Kinkhabwala & Thorsett 2000), and for both the giant pulses from PSR J1824−2452A at 1400 MHz and the Crab pulsar at 1300 MHz is $\alpha = 1.6$ (Knight et al. 2006; Bhat et al. 2008). Finding a similar value of $\alpha = 1.6$ also for RRAT J1819−1458 at 1540 MHz suggests that the emission mechanism of RRAT J1819−1458 is perhaps similar to that of pulsars with giant pulses. However, those detected giant pulses are from pulsars of relatively short spin periods measured in ms and have short pulse durations measured in μs even ns, which are quite different from those of RRAT J1819−1458. If the small amount of bursts of low intensities is not caused by observation sensitivity, the pulse intensity distribution of RRAT J1819−1458 may be similar to those of some normal pulsars (Hesse & Wielebinski 1974).

Both RRAT J1819−1458 and PSR B0656+14 have relatively high magnetic field strengths and moderate characteristic ages (Lyne et al. 2009; Becker & Trümper 1997), and similar X-ray emission properties are also observed for the

two neutron stars (McLaughlin et al. 2007; De Luca et al. 2005). The intensity CPD and emission modulation properties of RRAT J1819−1458 at ~1.5 GHz resemble those of B0656+14 at 327 MHz. Furthermore, the latter pulsar might have been observed as a RRAT if it had been at greater distance (Weltevrede et al. 2011, 2006). This indicates that RRAT J1819−1458 is possibly a normal pulsar with pulse properties similar to PSR B0656+14, while its quite large distance ensures that the former is detected as a pulsar with sporadic pulses. This may explain that most known RRATs have larger DM than most normal pulsars, since a large DM normally corresponds to a large distance that can ensure that the modulated pulses with low flux densities remain undetected. However, there is presently only one RRAT with $DM > 500$ pc cm^{-3}, which indicates an upper limit of DM because an excessively large distance would ensure that even extremely bright pulses of a neutron star remain invisible.

5. Conclusions

This paper has presented the analysis results of 423 detected bursts of RRAT J1819−1458. A value of $DM = 195.7 \pm 0.3$ pc cm^{-3} with 5σ error is obtained. A simple timing result is given and the tri-band shape of timing residuals is confirmed. Pulses situated in the central timing residual band are more complicated, including 27 bimodal bursts, the broadest burst, and the brightest one. The differences in the average SNR and average W_{50} of bursts in the two side residual bands are indicated. Profiles of four typical individual bursts including two bimodal bursts, and a plot of SNR versus W_{50} are presented. A possible power-law intensity CPD with index $\alpha = 1.6 \pm 0.2$ is measured.

Differences in both SNR and W_{50} of single pulses in the two side bands of timing residuals for RRAT J1819−1458 are briefly discussed. Comparisons between the flux intensity distribution and those of giant pulses, and, similarities in the emission properties of the RRAT and PSR B0656+14 are also briefly presented.

References

Becker, W., & Trümper, J. 1997, A&A, 326, 682
Bhat, N. D. R., Tingay, S. J., & Knight, H. S. 2008, ApJ, 676, 1200
Burke-Spolaor, S., & Bailes, M. 2010, MNRAS, 402, 855
Cognard, I., Shrauner, J. A., Taylor, J. H., & Thorsett, S. E. 1996, ApJ, 457, L81
Cordes, J. M., & McLaughlin, M. A. 2003, ApJ, 596, 1142
Cordes, J. M., & Shannon, R. M. 2008, ApJ, 682, 1152
De Luca, A., Caraveo, P. A., Mereghetti, S., Negroni, M., & Bignami, G. F. 2005, ApJ, 623, 1051
Deneva, J. S., Cordes, J. M., McLaughlin, M. A., et al. 2009, ApJ, 703, 2259
Deshpande, A. A., & Rankin, J. M. 1999, ApJ, 524, 1008
Dhillon, V. S., Marsh, T. R., & Littlefair, S. P. 2006, MNRAS, 372, 209
Esamdin, A., Zhao, C. S., Yan, Y., et al. 2008, MNRAS, 389, 1399
Gaensler, B. M., McLaughlin, M., Reynolds, S., et al. 2007, Ap&SS, 308, 95
Haberl, F. 2007, Ap&SS, 308, 181
Hankins, T. H., Kern, J. S., Weatherall, J. C., & Eilek, J. A. 2003, Nature, 422, 141
Hesse, K. H., & Wielebinski, R. 1974, A&A, 31, 409
Hobbs, G. B., Edwards, R. T., & Manchester, R. N. 2006, MNRAS, 369, 655
Karastergiou, A., Hotan, A. W., van Straten, W., McLaughlin, M. A., & Ord, S. M. 2009, MNRAS, 396, L95
Keane, E. F., & Kramer, M. 2008, MNRAS, 391, 2009
Keane, E. F., Ludovici, D. A., Eatough, R. P., et al. 2010, MNRAS, 401, 1057
Kinkhabwala, A., & Thorsett, S. E. 2000, ApJ, 535, 365
Knight, H. S., Bailes, M., Manchester, R. N., & Ord, S. M. 2006, ApJ, 653, 580
Kondratiev, V. I., McLaughlin, M. A., Lorimer, D. R., et al. 2009, ApJ, 702, 692
Li, X. 2006, ApJ, 646, L139
Lorimer, D. R., & Kramer, M. 2005, Handbook of Pulsar Astronomy (Cambridge University Press), 269
Luo, Q., & Melrose, D. 2007, MNRAS, 378, 1481
Lyne, A. G., & Graham-Smith, F. 2006, Pulsar Astronomy (Cambridge University Press), 26
Lyne, A. G., & Manchester, R. N. 1988, MNRAS, 234, 477
Lyne, A. G., McLaughlin, M. A., Keane, E. F., et al. 2009, MNRAS, 400, 1439
Manchester, R. N., Lyne, A. G., Camilo, F., et al. 2001, MNRAS, 328, 17
McLaughlin, M. A., Lyne, A. G., Lorimer, D. R., et al. 2006, Nature, 439, 817
McLaughlin, M. A., Rea, N., Gaensler, B. M., et al. 2007, ApJ, 670, 1307
McLaughlin, M. A., Lyne, A. G., Keane, E. F., et al. 2009, MNRAS, 400, 1431
Mereghetti, S. 2008, A&ARv, 15, 225
Ouyed, R., Leahy, D., Niebergal, B., & Yue, Y. 2009, MNRAS, 396, 1058
Popov, S. B., Turolla, R., & Possenti, A. 2006, MNRAS, 369, L23
Rea, N., McLaughlin, M. A., Gaensler, B. M., et al. 2009, ApJ, 703, L41
Rea, N., Curto, G. L., Testa, V., et al. 2010, MNRAS, 407, 1887
Reynolds, S. P., Borkowski, K. J., Gaensler, B. M., et al. 2006, ApJ, 639, L71
Serylak, M., Stappers, B. W., Weltevrede, P., et al. 2009, MNRAS, 394, 295
Wang, N., Manchester, R. N., Zhang, J., et al. 2001, MNRAS, 328, 855
Wang, N., Manchester, R. N., & Johnston, S. 2007, MNRAS, 377, 1383
Weltevrede, P., Stappers, B. W., Rankin, J. M., & Wright, G. A. E. 2006, ApJ, 645, L149
Weltevrede, P., Johnston, S., & Espinoza, C. M. 2011, MNRAS, 411, 1917
Woods, P. M., & Thompson, C. 2006, Compact stellar X-ray sources, ed. W. H. G. Lewin, & M. van der Klis (Cambridge University Press), 547
Zhang, B., Gil, J., & Dyks, J. 2007, MNRAS, 374, 1103